PACRG and FAP20 form the inner junction of axonemal doublet microtubules and regulate ciliary motility

Erin E. Dymek[a], Jianfeng Lin[b,†,‡], Gang Fu[b,†], Mary E. Porter[c], Daniela Nicastro[b], and Elizabeth F. Smith[a,*]

[a]Department of Biological Sciences, Dartmouth College, Hanover, NH 03755; [b]Departments of Cell Biology and Biophysics, University of Texas Southwestern Medical Center, Dallas, TX 75390; [c]Department of Genetics, Cell Biology and Development, University of Minnesota, Minneapolis, MN 55455

ABSTRACT **We previously demonstrated that PACRG plays a role in regulating dynein-driven microtubule sliding in motile cilia. To expand our understanding of the role of PACRG in ciliary assembly and motility, we used a combination of functional and structural studies, including newly identified *Chlamydomonas pacrg* mutants. Using cryo-electron tomography we show that PACRG and FAP20 form the inner junction between the A- and B-tubule along the length of all nine ciliary doublet microtubules. The lack of PACRG and FAP20 also results in reduced assembly of inner-arm dynein IDA *b* and the beak-MIP structures. In addition, our functional studies reveal that loss of PACRG and/or FAP20 causes severe cell motility defects and reduced in vitro microtubule sliding velocities. Interestingly, the addition of exogenous PACRG and/or FAP20 protein to isolated mutant axonemes restores microtubule sliding velocities, but not ciliary beating. Taken together, these studies show that PACRG and FAP20 comprise the inner junction bridge that serves as a hub for both directly modulating dynein-driven microtubule sliding, as well as for the assembly of additional ciliary components that play essential roles in generating coordinated ciliary beating.**

Monitoring Editor
Erika Holzbaur
University of Pennsylvania

Received: Jan 28, 2019
Revised: Apr 29, 2019
Accepted: May 16, 2019

INTRODUCTION

Data resulting from a combination of structural, biochemical, and functional studies of cilia using newly identified *Chlamydomonas* mutants have revealed a number of protein complexes located in distinct positions relative to the force-generating dynein arms, which play important and unique roles in ciliary assembly and modulation of ciliary motility (e.g., the nexin-dynein regulatory complex [N-DRC], CaM and spoke-associated complex [CSC], and MIA complex; Piperno *et al.*, 1994; King and Dutcher, 1997; Dymek and Smith, 2007). Reports from several labs indicate that PACRG is also an important component of a regulatory network essential for proper ciliary assembly and motility. PACRG, whose transcription is coregulated with the Parkinson's disease–related gene *parkin* (Kitada *et al.*, 1998; West *et al.*, 2003), has been localized to the ciliary axoneme (Dawe *et al.*, 2005; Lechtreck *et al.*, 2009; Thumberger *et al.*, 2012). Loss of PACRG results in male sterility (Lorenzetti *et al.*, 2004), defects in ependymal ciliary motility, and hydrocephalus in mice (Wilson *et al.*, 2009, 2010). RNA interference– and morpholino oligomer–mediated knockdown of the *PACRG* gene(s) in *Trypanosoma brucei* and *Xenopus*, respectively, results in impaired flagellar motility and defects in doublet microtubule (DMT) integrity (Dawe *et al.*, 2005). In vertebrates, knockdown of *PACRG* results in defects in left–right body axis, neural tube closure, and gastrulation (Thumberger *et al.*, 2012).

Several studies suggest a close relationship of PACRG and FAP20 with the DMTs. For example, PACRG binds directly to tubulin and microtubules (Ikeda, 2008). PACRG and FAP252 seem to interact with

This article was published online ahead of print in MBoC in Press (http://www.molbiolcell.org/cgi/doi/10.1091/mbc.E19-01-0063) on May 22, 2019.

†These authors contributed equally to this work.

‡Present address: Thermo Fisher Scientific, Materials & Structural Analysis, 5350 NE Dawson Creek Drive, Hillsboro, OR 97124.

*Address correspondence to: Elizabeth F. Smith (Elizabeth.f.smith@dartmouth.edu).

Abbreviations used: CA, central apparatus; cryo-ET, cryo-electron tomography; CSC, CaM and spoke-associated complex; DMT, doublet microtubule; DTT, dithiothreitol; EM, electron microscopy; HRP, horseradish peroxidase; IJ, inner junction; MIP, microtubule inner protein; N-DRC, nexin-dynein regulatory complex; PBS, phosphate-buffered saline; TAP, Tris acetate phosphate; WT, wild type.

the microtubule inner protein (MIP) Rib72 (Ikeda *et al.*, 2007). FAP20 is an inner junction (IJ) protein of the ciliary DMTs, and PACRG, but not Rib72, is reduced in *fap20* mutants (Yanagisawa *et al.*, 2014), indicating that FAP20 and PACRG may interact. *fap20* mutants (Yanagisawa *et al.*, 2014), like *pacrg* mutants (Wilson *et al.*, 2009, 2010), have cilia with abnormal motility. Taken together, these data suggest that PACRG and FAP20 may form a complex that is associated with the axonemal DMTs and that plays a role in regulating ciliary motility.

To study the structure and function of PACRG and FAP20 in more detail, we took advantage of *Chlamydomonas* mutants and employed cryo-electron tomography (cryo-ET) imaging and functional assays, such as the in vitro microtubule sliding assay. We definitively visualized that PACRG and FAP20 are arranged in an alternating pattern to form the IJ that links the A- and B-tubule protofilaments A1 and B10 of the axonemal DMTs. Our previous results showed that PACRG mediates regulatory cues from components of a signal transduction pathway that includes the central apparatus (CA), radial spokes (RSs), and specific inner dynein arms (Mizuno *et al.*, 2016). Here, we show that, in addition to being integral components of the DMT lattice, PACRG and FAP20 are required both for proper activation of dynein-driven microtubule sliding and for the assembly of other regulatory components that are key for coordinating dynein activity and thus generating ciliary motility.

RESULTS

Identification of *pacrg* mutants

Using an in vitro microtubule sliding assay and anti-PACRG antibodies, we previously demonstrated that PACRG plays a role in regulating dynein-driven microtubule sliding (Mizuno *et al.*, 2016). To expand our studies of PACRG function in ciliary motility, we characterized two *pacrg* mutants (159746 and 208023, referred to as "159" and "208," respectively) from the CLiP (*Chlamydomonas* Library Project) collection of insertional mutants (Li *et al.*, 2016; Cheng *et al.*, 2017). To verify that these strains carried an insertion in the gene encoding PACRG, we performed PCR using pairs of primers (Supplemental Figure S1 and Supplemental Table S1) along the length of the *PACRG* gene. We discovered that the CLiP 159 mutant is a complete knockout of the *PACRG* gene, because all PCRs along the entirety of the *PACRG* gene that were successful using control WT (WT) DNA, failed to amplify fragments from CLiP 159 genomic DNA. In contrast, the CLiP 208 mutant carries an insertion between exons 3 and 4 (Figure 1A).

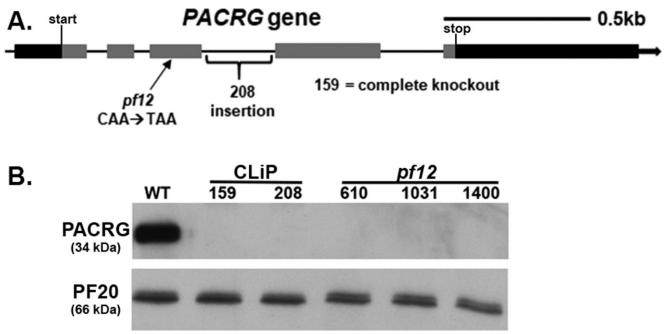

FIGURE 1: Identification of *pacrg* mutants in *Chlamydomonas*. (A) Diagram of the *PACRG* gene indicating the location of the CLiP and *pf12* mutations. Black indicates 5′ and 3′ untranslated region. Gray indicates exons. (B) An anti-PACRG Western blot of WT and *pacrg* mutant axonemes. PACRG protein was not detected in any of the mutant axonemes. PF20, a central pair protein, is used as a loading control.

The *PACRG* gene (Cre02.g113400) is located on the right arm of chromosome 2, approximately 550 kb away from the *LF1* gene (Cre02.g108950). Previous genetic mapping studies had also shown that *lf1* is closely linked to the motility mutant *pf12* (McVittie, 1972; Harris, 1989). As the mutant gene product of the *PF12* locus has not been previously identified, we suspected that the *pf12* mutations might also affect the *PACRG* gene. We therefore sequenced each of the three *pf12* mutants available from the *Chlamydomonas* resource center (cc610, cc1031, and cc1400) and found that the *PACRG* gene in each strain carried the same mutation. Specifically, each has a base pair change at nucleotide 316 of the third exon of the coding sequence (Figure 1A), which changes a glutamine (CAA) to a stop codon (TAA). As further verification, Western blots of isolated axonemes revealed that the PACRG protein could not be detected in axonemes isolated from either one of the two *pacrg* CLiP strains or the three *pf12* strains (Figure 1B).

PACRG is required for WT motility

All *pacrg* mutants have a severe motility defect. *Chlamydomonas* cells from CLiP *pacrg* mutant strains as well as the *pf12* strains cannot swim efficiently or produce WT waveforms (Figure 2B). The cilia of these cells twitch and jerk with uncoordinated movement (Supplemental Videos 1–3). A similar motility defect was described for *fap20* mutants in *Chlamydomonas*, which were also reported to have reduced levels of PACRG (Yanagisawa *et al.*, 2014). To confirm that the motility defect is due to the mutations in the *PACRG* gene, we transformed both CLiP strains and the *pf12* mutant with the WT *PACRG* gene. WT swim speed, beat frequency, waveforms, and assembly of PACRG were restored in all rescued strains tested (Figure 2).

Mutants axonemes lacking PACRG and FAP20 have reduced microtubule sliding velocity

To further investigate the cause of the motility defects in the *pacrg* and *fap20* mutants, we assessed microtubule sliding activity using isolated axonemes and an in vitro microtubule sliding disintegration assay to determine whether the lack of these proteins affects the coordination of dynein activity along the DMTs or the activity of the dynein arms themselves. The assay was applied to isolated axonemes of four mutant strains: one *pacrg* CLiP strain (159), one *pf12* mutant (*pf12*-cc1031), a *fap20* mutant, and a *pacrg; fap20* double-mutant strain.

No significant differences were observed between the 159 and *pf12* strains or between the respective rescued strains 159R and *pf12*R. Therefore, we refer to the *pf12* strain as the *pacrg* mutant and include data from this strain in Figure 3, Supplemental Figures S2 and S3, and Tables 1 and 2. We found that *pacrg* mutant axonemes have significantly slower sliding velocity than WT axonemes (WT = 17.1 ± 0.43 μm/s, *pacrg* = 14.13 ± 0.28 μm/s) (Figure 3 and Table 1). Sliding velocities of axonemes isolated from the rescued mutant strains (*pacrgR*) are not significantly different from that of WT (*pacrgR* = 16.96 ± 0.41 μm/s) (Figure 3 and Table 1).

Like the *pacrg* mutant, the *fap20* mutant axonemes have slow sliding velocities (13.95 ± 0.30 μm/s) compared with WT. Furthermore, sliding velocity is restored to WT levels upon transformation of the *fap20* mutant with the *FAP20* gene (17.09 ± 0.62 μm/s). The microtubule sliding velocities for the *pacrg; fap20* double mutant (13.40 ± 0.36 μm/s) were not significantly different from either single mutant ($p = 0.115$ compared with *pacrg*; $p = 0.237$ compared with *fap20*). These combined results indicate that dynein-driven microtubule sliding is equally affected by the loss of either PACRG or FAP20 and that PACRG and FAP20 may be components of a single structure or pathway affecting dynein activity.

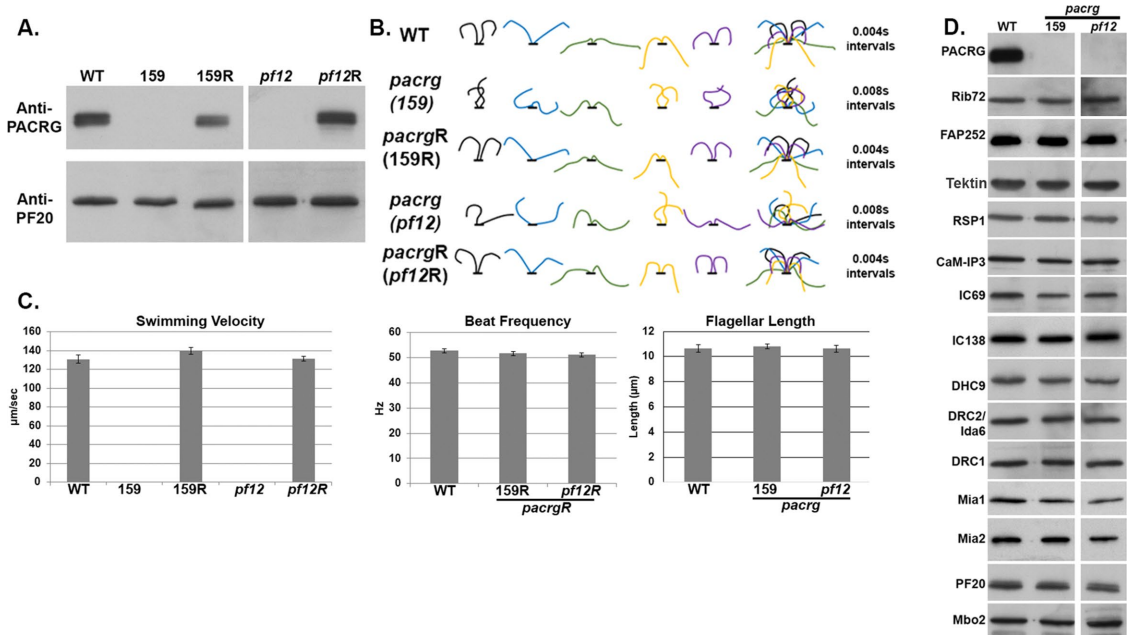

FIGURE 2: Motility defects of *pacrg* mutants are due to abnormal flagellar waveforms. (A) Anti-PACRG Western blots indicating PACRG protein is present in cells transformed with the WT PACRG gene. (B) Waveform tracings of flagella from WT, *pacrg* mutants (159 and *pf12*), and *pacrg* mutants rescued with the WT *PACRG* gene (159R and *pf12*R). (C) Histograms of swimming velocity, beat frequency, and flagellar length from WT, *pacrg* mutants, and *pacrg* mutants rescued with the WT *PACRG* gene. Beat frequencies were unable to be measured from *pacrg* mutants due to their abnormal waveform. (D) Western blots of axonemes from WT and *pacrg* mutants. Blots were probed with antibodies against proteins present on various known structures in the axonemes.

Addition of exogenous PACRG or FAP20 protein to the respective mutant axonemes increases microtubule sliding velocity

We then tested whether dynein activity could be restored by reconstituting mutant axonemes by the addition of exogenous PACRG and/or FAP20 protein. For these experiments, we used bacterially expressed and purified His-PACRG or His-FAP20 protein. For confirmation that the bacterially expressed proteins bind to mutant axonemes, the expressed protein was added to mutant axonemes in increasing amounts and Western blots were performed with samples from each binding experiment (Supplemental Figure S2 and Supplemental Table S3). Binding saturated when 2.5 μg of either His-PACRG or His-FAP20 was added to 25 μg of either *pacrg* or *fap20* mutant axonemes, respectively. These analyses suggest that binding of PACRG and FAP20 to mutant axonemes is specific.

To test whether the expressed protein restores function, we subjected reconstituted axonemes to the microtubule sliding disintegration assay. Axonemes from the CA mutant *pf18* (which lack the CA, have WT levels of PACRG, and have slow sliding velocities) were used as a control. We observed no increase in sliding velocity in the *pf18* control upon the addition of His-PACRG (Figure 3 and Table 1). In marked contrast, microtubule sliding velocities for the *pacrg* strains increased with increasing amounts of added His-PACRG (Figure 3, Table 1, and Supplemental Figure S2). Similarly, sliding velocities for *fap20* mutant strains increased with increasing addition of His-FAP20 protein (Figure 3, Table 1, and Supplemental Figure S3). For both the *pacrg* and the *fap20* mutants, the maximal sliding velocities of reconstituted axonemes were not significantly different from WT at the saturated concentration of exogenous protein ($p = 0.764$ for *pacrg* + PACRG; $p = 0.175$ for *fap20* + FAP20). It was reported that the *fap20* mutant also had reduced levels of PACRG protein (Yanagisawa *et al.*, 2014). Therefore, we added both expressed His-FAP20 and His-PACRG protein to *fap20* mutant axonemes; the sliding velocities were significantly faster in the reconstituted axonemes, but not significantly faster than *fap20* axonemes treated with expressed FAP20 protein alone ($p = 0.717$).

We also conducted reconstitution experiments with the *pacrg; fap20* double mutant. The addition of expressed PACRG protein did not significantly increase sliding velocity of *pacrg; fap20* mutant axonemes ($p = 0.71$). The addition of FAP20 did significantly increase sliding velocities compared with the double mutant ($p = 0.0004$); however, velocities were not restored to WT levels. In contrast, addition of both PACRG and FAP20 to double-mutant axonemes restored sliding velocities to WT level ($p = 0.271$ compared reconstituted double mutant with wild type). These combined results indicate that both proteins are necessary for WT dynein-driven microtubule sliding.

PACRG and FAP20 are components of the IJ of the axonemal DMTs

For an initial assessment of potential structural defects in mutant axonemes, we performed Western blots of isolated *pacrg* mutant axonemes using antibodies that recognize components of major axonemal complexes, such as the CA, RSs, N-DRC, inner dynein arm components, and the MIA complex, as well as Rib72 and FAP252, which have been implicated as PACRG interactors (Ikeda *et al.*, 2007; Yanagisawa *et al.*, 2014). With the exception of the PACRG protein, all components were present in seemingly WT abundance (Figure 2D). This result was also reported for the *fap20* mutant (Yanagisawa *et al.*, 2014).

We also performed plastic-section transmission electron microscopy of isolated *pacrg* mutant axonemes and were unable to identify any obvious axonemal defects (unpublished data). Therefore, we used cryo-ET to visualize structural defects in mutant axonemes at

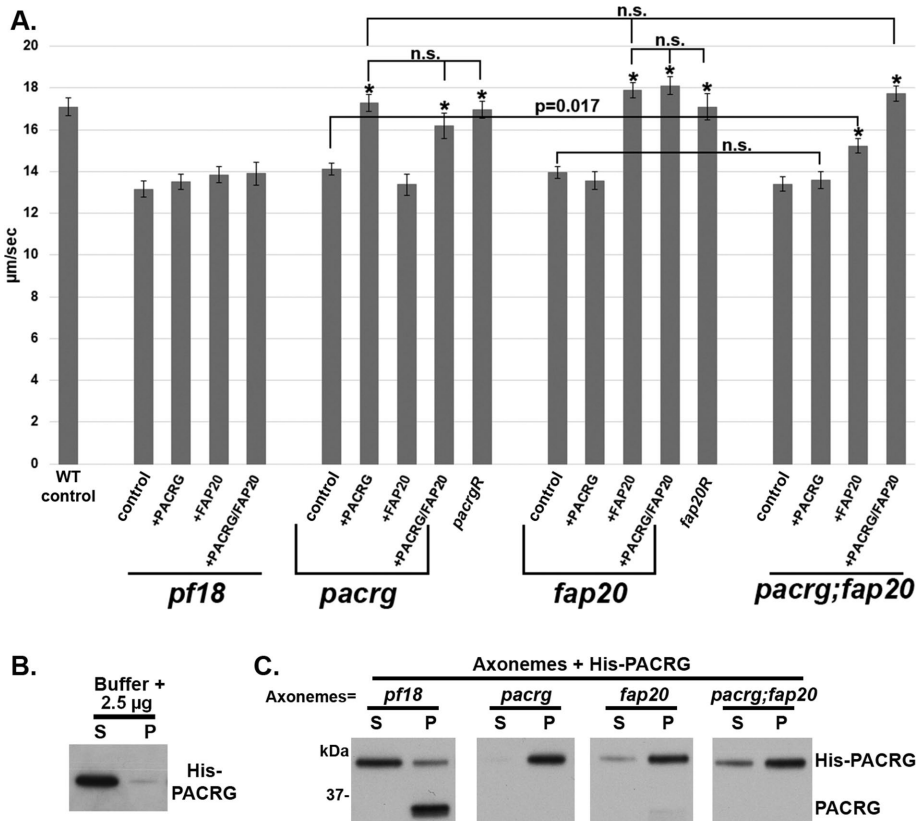

FIGURE 3: Microtubule sliding velocities are decreased in both *pacrg* and *fap20* mutants and can be restored to WT levels upon addition of their respective protein. (A) Compared with WT, the mutants *pacrg* (*pf12*), *fap20* (RL11), and *pacrg; fap20* have a significantly slower microtubule sliding velocity (Tables 1 and 2) in sliding buffer. This decrease in velocity is rescued upon the addition of 2.5 μg of purified expressed His-PACRG, His-FAP20, or both proteins to 25 μg of mutant axonemes. Axonemes from cells rescued with their WT gene (*pf12*R and *fap20*R) have sliding velocities similar to mutant axonemes with their WT expressed protein added (Tables 1 and 2). Axonemes from *pf18*, a central pair mutant, were used as a control. No increase in sliding velocity was observed with addition of either expressed protein. n.s., not significantly different; asterisk, significantly different than the same strain's value in sliding buffer.
(B) Pelleting assay control experiment using purified PACRG protein and buffer. Anti-PACRG Western blot of purified His-PACRG shows minimal His-PACRG pelleting (P) in the absence of axonemes. Most of the protein is found in the supernatant (S). (C) Pelleting assay using purified PACRG protein and isolated axonemes. Anti-PACRG Western blots of axonemes incubated with His-PACRG (25 μg of axonemes with 2.5 μg of His-PACRG) and pelleted. Most of the His-PACRG is found in the pellet (P) fraction, indicating that His-PACRG binds *pacrg*, *fap20*, and *pacrg:fap20* axonemes, all of which have no or minute amounts of PACRG endogenous protein. A small amount of His-PACRG pellets with *pf18* axonemes, which assemble PACRG protein, was used as a control. For complete results of the pelleting assay, see Supplemental Figure 2.

higher resolution (Supplemental Figure S4). A WT to mutant comparison of the averaged axonemal repeats from the *pacrg* mutant revealed a primary structural defect that was present in all axonemal repeats of the mutant, as well as partial reduction of two additional complexes that are likely secondary defects. The primary defect was consistently identified in the IJ between the A- and B-tubules of all outer DMTs of *pacrg* flagella (Table 3). We previously showed that, in WT axonemes, the IJ consists of repeated nontubulin subunits that leave a hole in the IJ close to the N-DRC base plate (Nicastro *et al.*, 2011). Here, we found that, in *pacrg* axonemes, every other subunit along the IJ was missing, including the subunit that is typically missing near the N-DRC (Figure 4, A–H). These structural defects were consistently observed in all 19 axonemes examined and on all nine DMTs of the axonemes (Supplemental Figure S5), making PACRG a likely key component of the IJ of the outer DMTs. Interestingly, the IJ is in close proximity to where the inner-arm dyneins of the neighboring DMT bind to the B-tubule protofilament B10 (Figure 4A).

Because FAP20 has previously been reported as an IJ protein (Yanagisawa *et al.*, 2014), we further compared the axonemal structure between WT and a *pacrg; fap20* double mutant. In the double mutant, the entire IJ between the A- and B-tubules was missing (Figure 4, I–L, Table 3, and Supplemental Figure S4). This suggests that the remaining IJ density observed in the *pacrg* mutant is FAP20, and that PACRG and FAP20 form the heterodimeric unit of the axonemal IJ in WT axonemes.

The lack of PACRG and FAP20 is associated with a reduction of inner-arm dynein IDA *b*, the I1-tether base, and the beak-MIP as secondary defects

In addition to the complete lack of a specific IJ component in a *pacrg* mutant or of both IJ components in the *pacrg; fap20* mutant, we noticed that the densities of three additional axonemal complexes were reduced in the averages of all axonemal repeats of these mutants compared with WT axonemes, namely, inner dynein *b* (Figure 5 and Supplemental Figure S6); the I1-tether base; and one of the MIP structures, the beak-MIP (Figure 6, Table 3, and Supplemental Figure S6). Interestingly, two of these structures, IDA *b* and beak-MIP, are known to be asymmetrically distributed among the nine doublets, as well as along the flagellar length (Hoops and Witman, 1983; Bui *et al.*, 2009; Nicastro, 2009). In addition, a previous study of *mbo* mutants noted a defect in the assembly of the B-tubule beak structures in the *pf12* mutant (Tam and Lefebvre, 2002). Therefore, we used classification analyses (Heumann *et al.*, 2011) focused on each complex to further dissect the structural defects, abundance, and distribution patterns of these structures in both WT and mutant flagella.

Consistent with previous studies (Bui *et al.*, 2012; Lin *et al.*, 2012), our analysis confirmed that, in WT axonemes, the inner-arm dynein IDA *b* varied both along the length of the flagellum and also in a doublet-specific pattern circumferentially, such that ~40% of the WT repeats lacked IDA *b*. More specifically, IDA *b* is missing from all doublets in the very proximal region, from DMTs 1, 5, and 9 in the midregion, and from doublets 1 and 9 in the distal regions (Figure 5F). In the *pacrg* mutant, considerably more axonemal repeats lacked IDA *b* also in the middle and distal region (overall 74% repeats lacking IDA *b*), with the greatest reduction observed on doublets 2–4 compared with wild type (Figure 5, G and H). The deficiency of IDA *b* is even more severe in the *pacrg; fap20* double mutant. Overall, 94% of the repeats lacked IDA *b* in the double mutant (Supplemental Figure S6), including 92% of the repeats in

Strain	Condition	μm/s ± SEM	*n*	*p* value[a]
WT	Control	17.10 ± 0.43	114	
pf18	Control	13.16 ± 0.40	108	
	+His-PACRG	13.51 ± 0.37	102	$p = 0.52$
	+His-FAP20	13.84 ± 0.39	105	$p = 0.22$
	+His-PACRG/-FAP20	13.91 ± 0.55	68	$p = 0.27$
pacrg (pf12)	Control	14.13 ± 0.28	130	
	+His-PACRG	17.29 ± 0.41	131	$p < 0.0001$
	+His-FAP20	13.37 ± 0.50	70	$p = 0.19$
	+His-PACRG/-FAP20	16.18 ± 0.62	69	$p = 0.004$
*pacrg*R	Control	16.96 ± 0.41	103	$p < 0.0001$
fap20 (RL11)	Control	13.95 ± 0.30	123	
	+His-PACRG	13.56 ± 0.42	68	$p = 0.45$
	+His-FAP20	17.78 ± 0.37	116	$p < 0.0001$
	+His-PACRG/-FAP20	18.10 ± 0.43	69	$p < 0.0001$
*fap20*R	Control	17.09 ± 0.62	85	$p < 0.0001$
pacrg; fap20	Control	13.40 ± 0.36	98	
	+His-PACRG	13.60 ± 0.41	95	$p = 0.71$
	+His-FAP20	15.23 ± 0.36	133	$p = 0.0004$
	+His-PACRG/-FAP20	17.73 ± 0.36	131	$p < 0.0001$

[a]Students's *t* test was used to determine the *p* value when comparing a condition's velocity to the control velocity of that same strain.

TABLE 1: Microtubule sliding velocities in control buffer or buffer with the indicated purified expressed protein added.

the mid- and distal regions. A similar classification analysis performed on a neighboring dynein, IDA *c*, did not show any differences in abundance or distribution between WT and *pacrg* axonemes (Supplemental Figure S7). These observations suggest that the differences observed in the assembly of IDA *b* are not related to the axoneme preparation (extraction rate) or classification method, but are specifically associated with the *pacrg* and *pacrg; fap20* mutations.

Another structure that is reduced or missing in the *pacrg* and *pacrg; fap20* mutant axonemes, respectively, is the I1 tether base

Samples compared	*p* value
WT vs. *pacrg*	$p < 0.0001$
WT vs. *fap20*	$p < 0.0001$
WT vs. *pacrg; fap20*	$p < 0.0001$
WT vs. *pacrg*R	$p = 0.817$
WT vs. *fap20*R	$p = 0.986$
WT vs. *pacrg* + His-PACRG	$p = 0.764$
WT vs. *fap20* + His-FAP20	$p = 0.175$
WT vs. *pacrg; fap20* + His-PACRG/His-FAP20	$p = 0.271$
pacrg; fap20 vs. *pacrg*	$p = 0.115$
pacrg; fap20 vs. *fap20*	$p = 0.237$
fap20 vs. *pacrg; fap20* + His-PACRG (both +PACRG, no FAP20)	$p = 0.498$
pacrg vs. *pacrg; fap20* + His-FAP20 (both +FAP20, no PACRG)	$p = 0.017$
pacrg + His-PACRG vs. *fap20* + His-FAP20 (both +PACRG, +FAP20)	$p = 0.273$
pacrg + His-PACRG vs. *pacrg; fap20* + His-PACRG/His-FAP20 (both +PACRG, +FAP20)	$p = 0.410$
fap20 + His-FAP20 vs. *pacrg; fap20* + His-PACRG/His-FAP20 (both +PACRG, +FAP20)	$p = 0.759$
pacrg + His-PACRG vs. *pacrg* + His-PACRG/His-FAP20 (both +PACRG, +FAP20)	$p = 0.141$
fap20 + His-FAP20 vs. *fap20* + His-PACRG/His-FAP20 (both +PACRG, +FAP20)	$p = 0.717$

TABLE 2: Student's *t* test values of various comparisons of microtubule sliding velocities.

	Strains		
	WT	*pacrg*	*pacrg; fap20*
IJ	IJ is formed by alternating PACRG and FAP20 subunits with a periodicity of 8 nm	FAP20 assembles into the IJ, but loss of PACRG leaves hole between the FAP20 subunit every 8 nm.	Loss of the entire IJ density and the B-tubule protofilament B10 is detached from the A-tubule.
IDA *b*	IDA *b* is absent from ~40% of axonemal repeats and shows asymmetric distribution both among DMTs and from proximal to distal (i.e., absent proximal, but present distal, except for selected DMTs (1, 5, 9). WT structures also reported by Bui *et al.* (2012); Lin *et al.* (2012).	IDA *b* is absent in ~74% of axonemal particles.	IDA *b* is absent in ~94% of axonemal particles.
B-tubule beak-MIP	Three ribbons attaching to protofilaments B3–5; present in ~32% of axonemal repeats with asymmetric distribution both among DMTs (preferred DMTs 1, 5, 6) and from proximal to distal (distal less). WT structures also reported by Hoops and Witman (1983); Nicastro *et al.* (2011); Bui *et al.* (2012).	Beak-MIP is reduced in size (mostly only at B5) and number (present in ~20% of axonemal particles).	Beak-MIP is reduced in size (mostly only at B5) and number (present in ~7% of axonemal particles).
I1 tether base	I1 tether base forms a microtubule attachment of the tether/tether head complex. WT structures also reported by Fu *et al.* (2018).	I1 tether base is reduced in size.	I1 tether base is completely missing in the averaged axonemal repeats.

TABLE 3: Summary of structural defects in *pacrg* and *pacrg; fap20* mutants.

structure (cyan in Figure 4). The I1 inner dynein is an important regulatory complex of ciliary motility (Wirschell *et al.*, 2007), and the I1 tether/tether head complex was shown to undergo bend direction–specific conformational changes (Lin and Nicastro, 2018). The I1 tether base structure is in close proximity to the tether/tether head ridge, which is formed by the C-termini of FAP43 and FAP44 and ends close to the IJ (Fu *et al.*, 2018).

A comparison of the nine DMTs of WT axonemes with those of *pacrg* or *pacrg; fap20* axonemes identified a reduction of the beak-MIP structure from DMTs 5 and 6 of the mutant axonemes (Supplemental Figure S5). The beak was previously identified as a doublet-specific structure of *Chlamydomonas* flagella (Hoops and Witman, 1983) that is attached to the inside wall of the B-tubule between protofilaments B4 and B5 of DMTs 1, 5, and 6 in the proximal three quarters of the flagellum (Hoops and Witman, 1983; Nicastro *et al.*, 2011; Bui *et al.*, 2012). To precisely characterize the structural difference in the beak-MIP structures in the mutants, we performed classification analyses on WT and mutant axonemes. Consistent with previous studies, our data detected a similar overall distribution of the beak-MIP in WT axonemes, but with additional and previously unresolved details (Figure 6). Specifically, the WT beak-MIP is a more complex and variable structure with up to three ribbons attaching to the three B-tubule protofilaments B3–B5 (Figure 6, C and D). Each ribbon has a "pearl-chain" appearance in cross-section (Figure 6C) and showed cross-linked filaments along the length of the axoneme (Figure 6D). At our current resolution, the classification analysis identified at least four classes of the beak-MIP structure that differ in size and ribbon and filament number in WT axonemes (classes 2–5; Figure 6, C–J and R). In the very proximal region of WT axonemes, almost all of the doublets contained beak-MIPs, whereas in the midregion beak-MIPs were detected only in doublets 1, 5, and 6, and very few beak-MIPs were detected in any doublets in the distal region (Figure 6R). In the *pacrg* axonemes, the beak-MIPs were considerably reduced in size, ribbon and filament number (mainly extending only from protofilament B5, class 4), and overall abundance with the greatest reduction observed on doublets 5 and 6 (Figure 6, K–Q and S). Similar to *pacrg* mutant axonemes, classification analysis of *pacrg; fap20* axonemes revealed that 93% of the axonemal repeats lacked the beak-MIP (class 1) and the remaining repeats (7%) possessed only the B5 ribbon (class 4) (Supplemental Figure S6). In contrast to the beak-MIP, all other MIP structures, including the major B-tubule MIP3 (bridging between B9 and B10 close to the IJ), appeared unaffected in the *pacrg* and double-mutant axonemes. The fact that the IDA *b* and beak-MIP structures were not consistently missing from all the axonemal repeats in the *pacrg* mutant strongly suggests that these defects are secondary defects and may further indicate that the IJ plays a role in stabilizing the assembly of IDA *b* and the beak-MIP into the axoneme.

DISCUSSION

To expand our understanding of the role of PACRG in ciliary assembly and motility, we used a combination of functional and structural studies. We identified *pacrg* mutants in the CLiP library and discovered that the mutation in the previously identified *pf12* mutants occurs in the *pacrg* gene. For all *pacrg* mutants studied here, we showed that no PACRG protein is assembled into cilia and that all mutants have severely defective motility. Our results using isolated axonemes and a sliding disintegration assay indicate that the motility defect is due, at least in part, to altered dynein-driven microtubule sliding. We demonstrate that in vitro reconstitution of mutant axonemes with expressed PACRG protein rescues microtubule

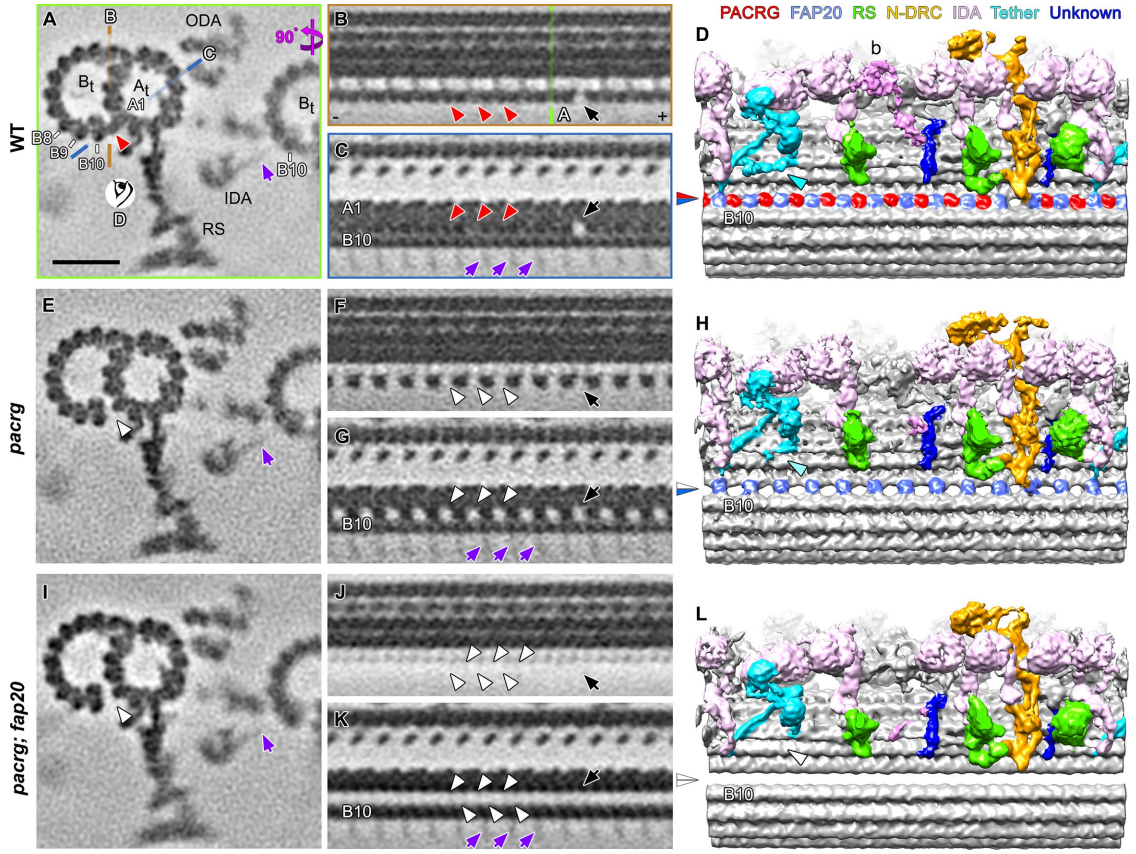

FIGURE 4: Cryo-ET of the *Chlamydomonas pacrg* and *pacrg; fap20* mutants reveals structural defects in the IJ of the DMTs. (A–L) Subtomogram averages of the axonemal repeats from WT (A–D), the *pacrg* mutant (E–H), and the *pacrg; fap20* double mutant are shown as cross-sectional (A, E, I; 3 nm thick) and two longitudinal (B, C, F, G, J, K; 2 nm thick) tomographic slices and as longitudinal three-dimensional isosurface renderings (D, H, L). The locations of the tomographic slices shown in B and C (orange and blue lines) and the viewing direction of D (eye symbol) are indicated in A, whereas the location of slice shown in A is indicated in B (green line). Densities that were present in WT axonemes but missing from *pacrg* and *pacrg; fap20* are highlighted by red and white arrowheads, respectively. The blue/red arrowhead in D indicates the WT IJ consisting of repeating PACRG/FAP20 heterodimers, which was missing the PACRG subunit in the *pacrg* mutant (blue/white arrowhead in H) or the entire IJ density in *pacrg;fap20* mutant (white/white arrowhead in L). Note that the I1 tether base structure (Fu *et al.*, 2018) present in WT (cyan arrowhead in D) is reduced in *pacrg* (H) and missing in *pacrg; fap20* (white arrowhead in L). The protofilaments (A1, B8–10) are numbered according to the prevailing numbering system (Linck and Stephens, 2007). Other labels: A_t, A-tubule; B_t, B-tubule; N-DRC, nexin-dynein regulatory complex; RS, radial spoke; ODA, outer dynein arm; + and – end, microtubule polarity; black arrow, IJ hole. Note the densities of the stalk and microtubule-binding domains of the inner dynein arms (IDAs) from the neighboring DMT bound to protofilament B10 (purple arrows in A, C, E, G, I, K). These densities are weak and exhibit an 8-nm periodicity, because 1) dyneins on the neighboring DMT n-1 bind to a specific site on the tubulin dimers on the DMT n, but 2) the position of axonemal repeats on the DMT n that are averaged vary among the nine DMTs of a flagellum. Scale bar: 20 nm (A, valid for all tomographic slices).

sliding velocity, indicating that the loss of dynein activity per se is due solely to the loss of PACRG. Notably, this exogenous addition of PACRG to isolated axonemes did not result in reactivation of beating. This is likely due to the secondary defects in the *pacrg* mutant—the reduced assembly of IDA *b* and the beak-MIP structures—suggesting that the latter structures are required for coordination of microtubule sliding to produce productive ciliary waveforms (discussed later). This is supported by the complete restoration of motility following transformation of *pacrg* mutants with the WT *PACRG* gene.

Our cryo-ET analyses of *pacrg* and *pacrg; fap20* axonemal structures revealed that PACRG and FAP20 are the primary components of the IJ, bridging protofilaments A1 and B10 along the length of all nine ciliary DMTs. While there are additional structural defects in the *pacrg* mutant, only the IJ defect is observed in 100% of axonemal repeats, making this the primary defect. Classification analyses demonstrated that the other, non-IJ defects are partial and heterogeneous (see Figures 5 and 6) and are therefore secondary defects. This is in contrast to a previous study that reported PACRG assembled on only a subset of DMTs (Lechtreck *et al.*, 2009). However, in these experiments, hemagglutinin-tagged PACRG was exogenously expressed in a WT strain, resulting in a mixture of tagged and untagged PACRG that could have given the appearance of assembly on selective DMTs. Alternating subunits of PACRG and FAP20 repeat continuously along the DMT with an axial periodicity of 8 nm, with the exception of one missing PACRG subunit every 96 nm near

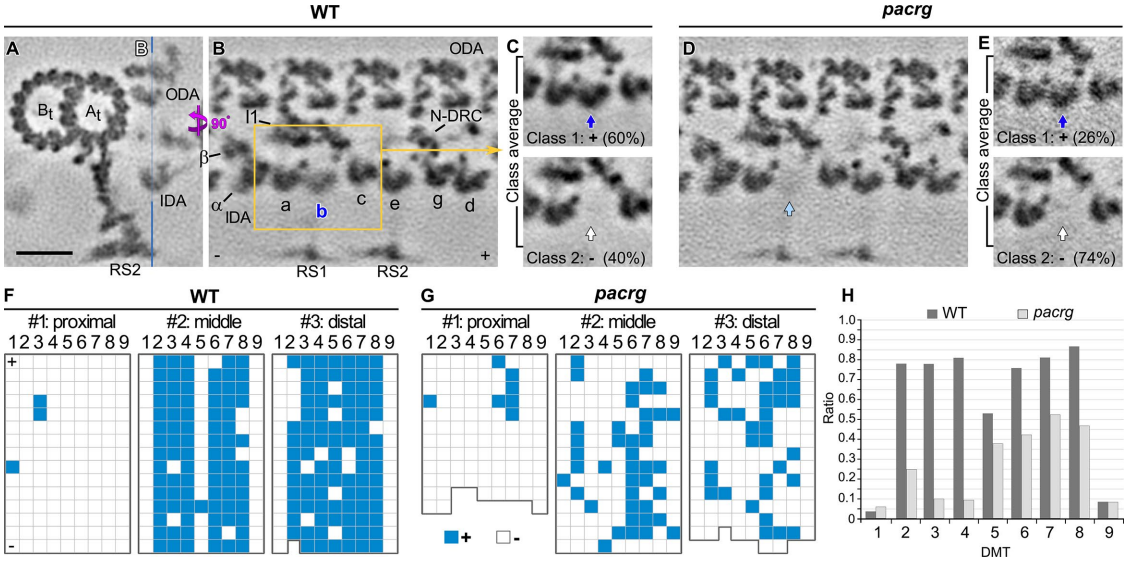

FIGURE 5: Classification analyses identified a (secondary) structural defect of missing inner-arm dynein *b* in the *Chlamydomonas pacrg* mutant. (A–E) Cross-sectional (A, 2 nm thick) and longitudinal (B–E, 5 nm thick) tomographic slices of the averaged axonemal repeats of WT (A–C) and *pacrg* axonemes (D, E) show that, in the mutant, more axonemal repeats are missing the inherently asymmetrically distributed IDA *b*. Averages of all repeats (A, B, D) show a typically reduced (B) or in the mutant mostly missing (D) density of IDA *b*; the class averages (C, E, classification focused on IDA *b*) clearly separate repeats with (class 1) and without (class 2) IDA *b* (blue, light blue, and white arrows), showing a greater reduction of IDA *b* in the mutant than WT; the percentage of each class average is indicated. The location of longitudinal slices is indicated in A (blue line). (F, G) Distributions of axonemal repeats with (blue grids) and without (white grids) IDA *b* in three different regions of individual flagella of WT (F) or *pacrg* mutant strains (G). In the distribution patterns, the repeats on the nine DMTs (1–9) are schematically shown as individual grids. (H) The histograms depict the ratios of repeats with IDA *b* relative to all repeats on individual DMTs ($n = 19$ axonemes). Microtubule polarity (+ and – end). Scale bar: 20 nm (A–E).

the N-DRC base plate (Figure 4). We previously described this "IJ hole" in WT DMTs of a wide range of species, from *Chlamydomonas* to human cilia (Heuser *et al.*, 2009; Nicastro *et al.*, 2011). Although a slight reduction of PACRG was reported in *fap20* mutant (Yanagisawa *et al.*, 2014), the FAP20 density was consistently observed in the *pacrg* mutant (Figure 4H). Evidently, each protein can assemble independent of the other. Interestingly, both subunits are required for WT dynein-driven microtubule sliding velocities (Figure 3).

Our structural and functional comparisons between WT and mutant DMTs also indicate that the IJ is an essential regulatory hub interacting with multiple axonemal complexes that are involved in regulating ciliary motility (summarized in Table 3). Two major regulatory complexes that seem to interact with the IJ are the N-DRC base plate and the CSC. A close relationship of these complexes with the IJ is supported by previous findings that the IJ hole is not observed, that is, it is likely filled with PACRG subunits, in selected *csc* and *drc* mutants (Heuser *et al.*, 2009, 2012). Another structure that was reduced or missing in the *pacrg* and *pacrg; fap20* mutants, respectively, is the I1 tether/tether head complex (Figure 4), which is critical for I1 dynein regulation (Fu *et al.*, 2018) and thus might affect the activity of I1 dynein in the mutants studied here. Two additional, so far uncharacterized structures (blue-colored densities in Figure 4, D, H, and L), seem to connect to the IJ. Although these structures retain a wild type–like morphology in the *pacrg* and *pacrg; fap20* mutant axonemes, one of these structures is associated with the tail domain of IDA *b*, which is reduced in the mutants studied here. Direct connections between these axonemal structures and the IJ suggest that the IJ could serve as a hub for integrating regulatory signals. In addition, the microtubule-binding domains of most IDAs connect to the B-tubule protofilament B10 right next to the IJ of the neighboring DMT. Therefore, it is possible that the IJ may plays a role, for example, stabilizing the position or rigidity, or regulating the amount of poly-glutamylation of protofilament B10, which is important for generating efficient sliding between neighboring DMTs (Kubo *et al.*, 2010; Suryavanshi *et al.*, 2010; Mendes Maia *et al.*, 2014).

The IJ proteins are required for the assembly of doublet-specific structures—the beak-MIP and IDA *b*. The protein component(s) of the beak-MIP remain unknown; however, the asymmetric planar stroke waveform observed for WT *Chlamydomonas* cells is disrupted in mutants lacking the beak-MIP, such as *fap20* and *mbo1* (Segal *et al.*, 1984; Meng *et al.*, 2014; Yanagisawa *et al.*, 2014). Our findings that *pacrg* mutants have reduced beak structures, particularly at DMT5 and DMT6 (Figure 6 and Supplemental Figure S6), and display abnormal waveform (Figure 2) provide additional support for the hypothesis that the beak-MIP is required to generate WT waveforms in *Chlamydomonas*. However, the fact that PACRG, FAP20, and MBO protein are not components of the beak structure suggests that other axonemal structures, reduced or missing in these mutants, may also control waveform. One possible structure found significantly reduced in *pacrg* and *pacrg; fap20* compared with WT is IDA *b* (Figure 5 and Supplemental Figure S6). In general, the IDA system regulates the propagation of ciliary waveform through physical interactions with various regulators of ciliary motility (Kamiya *et al.*, 1991; King, 2016). Our classification analyses revealed that other IDAs, such as IDA *c*, were unaffected in the *pacrg* axoneme (Supplemental Figure S7), suggesting that the reduction of IDA *b* may contribute to the altered waveform. Taken together, the intrinsic asymmetry of the assembled axonemal complexes such as beak-MIP and IDA *b* provide a structural basis for generating specific ciliary waveforms. Indeed, our recent study of active sea

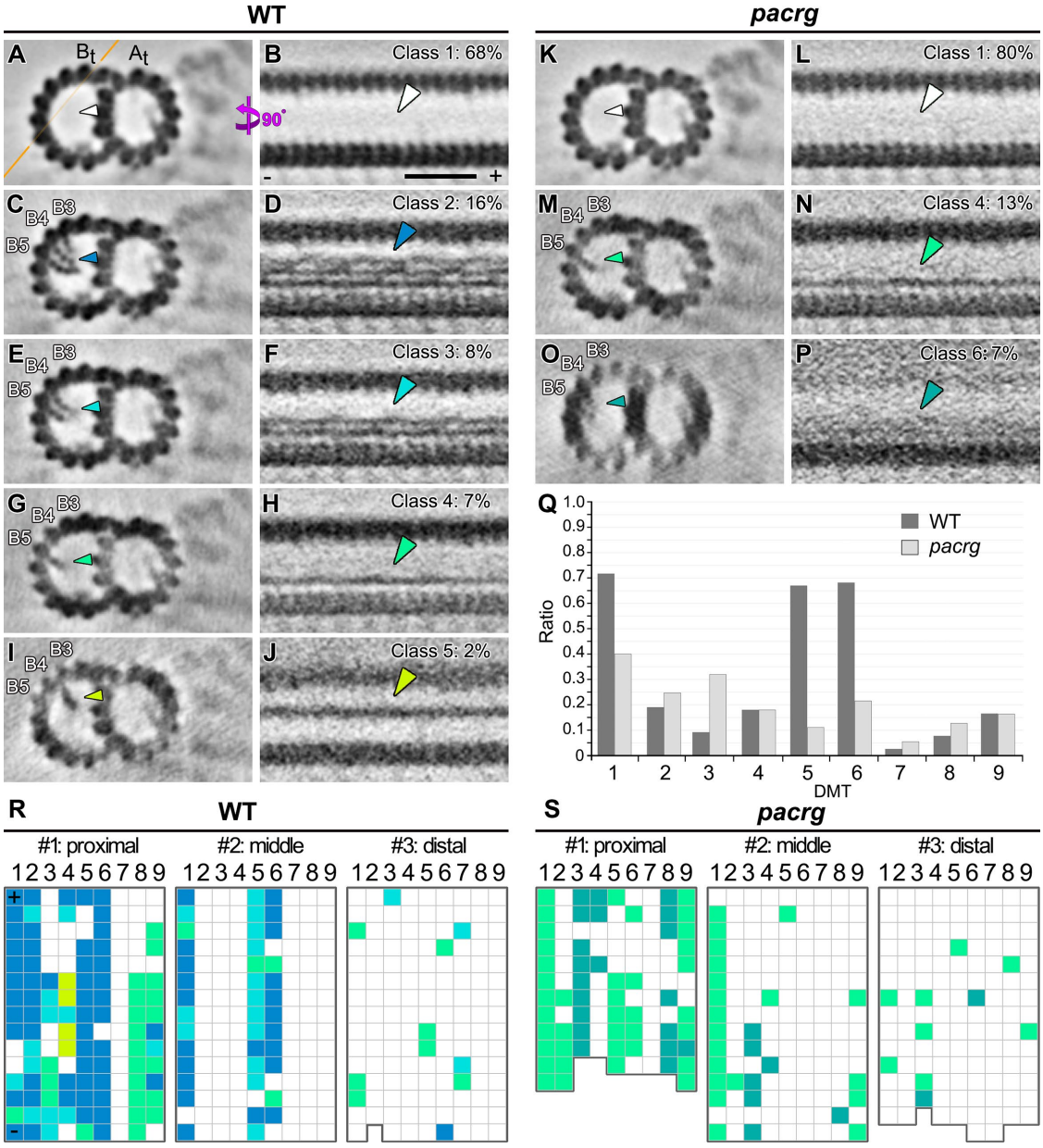

FIGURE 6: Classification analyses identified (secondary) structural defects of the beak-MIP in the B-tubules of the *Chlamydomonas pacrg* mutant DMTs. (A–P) Cross-sectional (left, 50 nm thick) and longitudinal (right, 5 nm thick) tomographic slices of the class-averaged axonemal repeats show DMTs without beak-MIP (class 1) and four normal classes (classes 2–5) of beak-MIP structures in WT (A–J) and defective beak-MIPs in *pacrg* axonemes (K–P), respectively. The location of the longitudinal slice is indicated by an orange line in A. Arrowheads with specific colors highlight the beak-MIP densities in different class averages, whereas the white arrowheads indicate lack of a beak-MIP; the percentage of each class average is indicated. The protofilaments (B3–5) are numbered according to the prevailing numbering system (Linck and Stephens, 2007). (Q) The histograms depict the ratios of repeats with beak-MIP structure relative to all repeats on individual DMTs (1–9) ($n = 19$ axonemes). (R, S) Distributions of axonemal repeats with (color grids) and without (white grids) beak-MIP structure in three different regions of individual flagella of WT (R) or *pacrg* mutant strain (S), respectively. In the distribution patterns, the repeats on the nine DMTs (1–9) are schematically shown as individual grids; grid coloring is consistent with the arrowhead colors in A–P. Microtubule polarity (+ and – end). Scale bar: 20 nm (A–P).

urchin sperm revealed the asymmetric distribution of dynein conformations, which correlate with bend direction (Lin and Nicastro, 2018).

The IJ is near microtubule inner proteins MIP3 and MIP6 and likely interacts with their associated proteins. MIP3a is composed of FAP52 and is an arch-shaped structure connecting protofilaments B9 and B10 (Nicastro *et al.*, 2011; Owa *et al.*, 2019). Our cryo-ET findings show that defects in the IJ in *pacrg* and *pacrg; fap20* mutants do not affect the stable assembly of MIP3a (Figure 4, E and I). Owa *et al.* (2019) report that the loss of FAP20 and FAP52 in a *fap20; fap52* double mutant results in significantly shorter and essentially paralyzed cilia, and classical electron microscopy (EM) images

showed a detachment of the B-tubule from the A-tubule in several DMTs (Owa *et al.*, 2019). The latter B-tubule detachment resembles the loss of the IJ density, as observed in our *pacrg; fap20* mutant. However, we found open B-tubules in *all* DMTs of the *pacrg; fap20* mutant (Figure 4 and Supplemental Figure S5), indicating that the IJ (PACRG and FAP20) serves to stably anchor the B-tubule to the A-tubule. Whereas the IJ interacts directly with MIP3a, it may indirectly interact with MIP6 in the A-tubule through the connection with protofilament A1. Our studies and others have revealed that MIP6 spans protofilaments A13-1-2-3 (Maheshwari *et al.*, 2015; Ichikawa *et al.*, 2017; Stoddard *et al.*, 2018). The possible association of PACRG with Rib72 was demonstrated by immunoprecipitation (Ikeda *et al.*, 2007). Our structural data revealed that Rib72 is associated with protofilaments A11-12-13-1 (Linck *et al.*, 2014), and loss of Rib72A/B affects the stability of MIP6 in *Tetrahymena* (Stoddard *et al.*, 2018). These combined data support the presence of a local "IJ (PACRG/FAP20)-A1-MIP6 (Rib72)" interaction within the ciliary DMTs. However, our studies and others (Yanagisawa *et al.*, 2014) have shown that Rib72 is present in WT amounts in the *fap20* and *pacrg* mutants, indicating that neither PACRG nor FAP20 is required for Rib72 assembly. As discussed in our previous study, the IJ plays a role in closing the B-tubule after its formation has been initiated from the outer junction (Nicastro *et al.*, 2011); however, whether the IJ binds first to protofilaments B10 or A1 remains unknown. Additional work will likely reveal the role of these proteins in the formation and stability of ciliary DMTs.

MATERIALS AND METHODS

Chlamydomonas reinhardtii strains and transformation

A54-e18 (*nit1-1*, *ac17*, *sr1*, *mt+*) and *cw15* (cc4533) were used as axonemal WT strains (*Chlamydomonas* Resource Center, University of Minnesota). PACRG insertional mutant strains (159746 and 208023) were obtained from the *Chlamydomonas* Library Project (CLiP, Jonikas lab; Li *et al.*, 2016). The CLiP strains ("159" and "208"), *pf12* strain (cc1031, cc610, and cc1400), *fap20* mutant (RL11 cc2993), and *pf18* were obtained from the *Chlamydomonas* Resource Center. Both CLiP 159 and 208 were backcrossed to confirm the motility phenotype and paromomycin-resistance phenotype cosegregated. RL11 was also backcrossed upon receipt and before conducting experiments using this strain. The *pacrg; fap20* double mutant was generated by mating RL11 and *pf12*. Meiotic progeny were screened for the absence of PACRG protein by Western blotting of flagella and for the presence of the RL11 *fap20* mutation by sequencing amplified genomic DNA (Yanagisawa *et al.*, 2014). All cells were grown in constant light in Tris acetate phosphate (TAP) media (Gorman and Levine, 1965).

The glass bead method was used for transformations. DNA (genomic clones containing the WT *PACRG* or *FAP20* genes) was cotransformed into cells with a plasmid containing a selectable marker: for *pf12*, the *APHVIII* gene, which confers paromomycin resistance; and for CLiP 159/208, the pHyg3 plasmid, which confers resistance to hygromycin B. Transformations were plated onto TAP + 20 μg/ml paromomycin plates or TAP + 50 μg/ml hygromycin B plates and placed in light. Colonies were picked into liquid TAP, and cells were screened for rescued motility.

Identification of the PACRG mutation in *pf12*

We isolated genomic DNA from the three strains identified as *pf12* mutations in the collection at the *Chlamydomonas* Resource Center (CC-1031, CC-1400, and CC-610). Genomic DNA was purified by standard phenol/chloroform extraction and ethanol precipitation protocols, and the *PACRG* gene (Cre02.g113400) was amplified using the Epicentre Fail Safe PCR system (Madison, WI) with their buffer G and the oligonucleotide primers listed in Supplemental Table S2. The PCR products were purified using the Promega Wizard SV PCR/Gel Clean-up system (Madison, WI) and sequenced by GeneWiz (Plainfield, NJ). All three strains showed the same single-base-pair mutation (CAA>TAA) that leads to a stop codon in the third exon at amino acid residue 106 of the PACRG polypeptide sequence. We therefore chose the CC1031 strain as the representative *pf12* mutant allele for this paper.

Axoneme isolation and Western blot analysis

Flagella were isolated using the dibucaine method (Witman, 1986). After the addition of 0.5% NP-40, axonemes were pelleted, resuspended at 1 mg/ml in NaLow (10 mM HEPES pH7.5, 5 mM $MgSO_4$, 1 mM dithiothreitol [DTT], 0.5 mM EDTA, and 30 mM NaCl) and fixed for gels. Axonemes (10 μg) were separated using SDS–PAGE and transferred to polyvinylidene fluoride for Western blotting or streptavidin overlays.

Blots were blocked for 1 h in 5% milk/TTBS (0.1% Tween,1X TBS) and incubated in TTBS plus antibody overnight at 4°C (see Supplemental Table S4 for antibodies and dilutions). After being washed with TTBS, blots were incubated with secondary antibody (anti-rabbit horseradish peroxidase [HRP] or anti-mouse HRP; GE Healthcare), diluted in TTBS for 30 min, and washed with TTBS. The ECL Prime kit (GE Healthcare) was used for detection.

PACRG and FAP20 genomic and cDNA vectors

A genomic clone of *PACRG* was synthesized in the pUC57 vector by GenScript (Piscataway, NJ). An *FAP20* genomic clone was made by amplifying the WT gene by PCR and inserting the PCR product into the pCR2.1 vector (Life Technologies/Thermo Fisher Scientific).

The cDNA clones of *PACRG* and *FAP20* were generated using reverse transcription-PCR. The amplified products for each were inserted into the pET30a expression vector and sequenced to verify orientation and reading frame. For expression, *PACRG*- or *FAP20*-pET30a was transformed into BL21(DE3)pLysS cells (Novagen) and induced using isopropyl β-d-1-thiogalactopyranoside. Expressed protein was purified using His Resin (Novagen) and dialyzed into 1X phosphate-buffered saline (PBS).

His-PACRG and His-FAP20 binding to axonemes

After purification and dialysis into PBS, 2.5 μg of His-PACRG, 2.5 μg of His-FAP20, or both were added to 25 μg of isolated axonemes in a total of 100 μl of buffer "klow" (10 mM HEPES pH7.5, 5 mM $MgSO_4$, 1 mM DTT, 0.5 mM EDTA, and 50 mM potassium acetate) and incubated for 15 min at room temperature to allow for binding. For the microtubule sliding assay, axonemes with bound protein were added to a chamber slide and washed with klow buffer to remove excess expressed protein. The microtubule sliding assay was carried out as described in the following section.

Microtubule sliding assay

Measurements for sliding microtubules were based on the method of Okagaki and Kamiya (1986), and standard sliding buffer ("klow" pCa8) was used for the assay. An AxioSkop 2 microscope (Zeiss) equipped for dark-field optics with a Plan-Apochromat 403 oil-immersion objective lens with iris and an ultra–dark field oil-immersion condenser was used for imaging. An ORCA-Flash 4.0 V2 (Hamamatsu) camera captured images, and Nikon NIS-Elements was used to record videos and measure sliding velocities. All data are presented as the mean ± SEM. At least three independent

experiments were performed for each strain. Student's *t* test was used for the comparison of two independent groups.

Video microscopy for motility analyses

A pco.1200HS camera with Camware software (Cooke, Londonderry, NH) was used to capture videos of motile cells. Videos and montages were created in ImageJ (Schneider *et al*., 2012). Swimming velocities, beat frequencies, and flagellar lengths were also measured in ImageJ.

Cryo-sample preparation

Axonemal samples used for cryo-ET were prepared, imaged, and processed as previously described (Fu *et al*., 2018). Briefly, *Chlamydomonas* cells (Supplemental Table S5) were grown in liquid TAP medium at 23°C under a light/dark cycle of 12:12 h with filtered air bubbling into the culture. Flagella were detached from the cells using the pH-shock method (Witman, 1986) and purified by two centrifugations (2400 rpm for 10 min) over 20% sucrose cushions. The flagellar membrane was removed by a 20-min incubation in demembranation buffer that contains 30 mM HEPES (pH 8.0), 25 mM KCl, 5 mM $MgCl_2$, 0.1 mM EDTA, 0.2 mM EGTA (ethylene glycol-bis(2-aminoethyl ether)-*N*,*N*,*N*′,*N*′-tetraacetic acid), and 1% IGEPAL CA-630 (Sigma-Aldrich, St. Louis, MO). The axonemes were collected by centrifugation at 10,000 × *g* for 10 min and resuspended in HMEEK buffer (30 mM HEPES, pH 7.4, 5 mM $MgSO_4$, 1 mM EGTA, 0.1 mM EDTA, and 25 mM KCl). Three microliters of the axoneme sample and 1 µl of 10-fold concentrated bovine serum albumin–coated 10-nm colloidal gold solution (Iancu *et al*., 2006) were applied to a glow-discharged (–30 mA for 30 s) Quantifoil holey carbon grid (R2/2, Quantifoil Micro Tools GmbH, Germany), which was loaded on a homemade plunge-freezing device. Excess buffer was blotted from the back side of the grid using Whatman filter paper (No.1) for 1.5–2.5 s, and then the grid was immediately plunge-frozen in liquid ethane. The frozen grids were stored in liquid nitrogen until used.

Cryo-ET

Vitrified samples were transferred into a Titan Krios transmission electron microscope (Thermo Fisher Scientific, Waltham, MA) operated at 300 keV. Axonemes that appeared well preserved (e.g., not compressed) by EM inspection were imaged using both a Volta-Phase-Plate at –0.5 µm defocus, making contrast transfer function correction unnecessary (Danev *et al*., 2014), and an energy filter in zero-loss mode (20-eV slit width; Gatan, Pleasanton, CA). Tilt series were recorded with a dose-symmetric scheme (Hagen *et al*., 2017) (–60° to +60° with 2° increments) using the microscope control software SerialEM (Mastronarde, 2005). The cumulative electron dose per tilt series was limited to ~100 e/Å^2. All images were digitally recorded on a K2 direct electron detector (Gatan, Pleasanton, CA) with a dose rate of 8 electrons/pixel per second in counting mode and at a nominal magnification of 26,000×, resulting in a pixel size of 0.5 nm.

Image processing

The movie frames of each tilt series image were aligned (motion corrected) and then summed using the script extracted from the IMOD software package (Kremer *et al*., 1996). The tilt series images were then aligned using fiducial markers and reconstructed into a three-dimensional tomogram by weighted back-projection using the IMOD software package. Tomograms of intact and noncompressed axonemes were used for subtomogram averaging of the 96-nm axonemal repeat units (volume size: 110 × 84 × 80 nm) to improve the resolution. Extracted repeats were aligned and averaged (including missing wedge compensation) using the PEET program (Nicastro *et al*., 2006). For doublet-specific averaging, the nine outer DMTs were identified based on previously reported doublet-specific features (Bui *et al*., 2012; Lin *et al*., 2012), and repeats from individual outer DMTs were averaged. To further analyze structural defects that appeared heterogeneous, we performed classification analyses on the aligned subtomograms using a clustering approach (principal component analysis) built into the PEET program (Heumann *et al*., 2011) with appropriate masks that were applied to focus the classification on structures of interest. Subtomograms that contained the structure of interest were grouped into class average. Using the information provided by the classification analysis, the structural defects were further mapped onto the respective location in the raw tomograms to characterize the distribution of structural classes. The numbers of tomograms and subtomograms analyzed are summarized in Supplemental Table S5. The resolution of the resulting averages (Supplemental Table S5) was estimated at the base of RS 1 using the Fourier shell correlation method with a criterion of 0.5. The structures were visualized as two-dimensional tomographic slices and three-dimensional isosurface renderings using IMOD and UCSF Chimera (Pettersen *et al*., 2004), respectively.

ACKNOWLEDGMENTS

We thank Douglas Tritscher (University of Minnesota) for his contribution to the sequence analysis of the *pf12* strains. We thank Daniel Stoddard (UT Southwestern Medical Center) for management of the electron microscope facilities and training. The UT Southwestern Cryo-Electron Microscopy Facility is supported in part by the CPRIT Core Facility Support Award RP170644. The three-dimensional averaged structures in this study have been deposited in a public database, namely EMDataResource, with the accession codes EMD-0628, EMD-0629 and EMD-0630. This study was funded by the following grants: National Institutes of Health R01GM112050 to E.F.S., R01GM083122 to D.N., and R01GM055667 to M.P.

REFERENCES

Bui KH, Sakakibara H, Movassagh T, Oiwa K, Ishikawa T (2009). Asymmetry of inner dynein arms and inter-doublet links in *Chlamydomonas* flagella. J Cell Biol 186, 437–446.

Bui KH, Yagi T, Yamamoto R, Kamiya R, Ishikawa T (2012). Polarity and asymmetry in the arrangement of dynein and related structures in the *Chlamydomonas* axoneme. J Cell Biol 198, 913–925.

Cheng X, Liu G, Ke W, Zhao L, Lv B, Ma X, Xu N, Xia X, Deng X, Zheng C, Huang K (2017). Building a multipurpose insertional mutant library for forward and reverse genetics in *Chlamydomonas*. Plant Methods 13, 36.

Danev R, Buijsse B, Khoshouei M, Plitzko JM, Baumeister W (2014). Volta potential phase plate for in-focus phase contrast transmission electron microscopy. Proc Natl Acad Sci USA 111, 15635–15640.

Dawe HR, Farr H, Portman N, Shaw MK, Gull K (2005). The Parkin co-regulated gene product, PACRG, is an evolutionarily conserved axonemal protein that functions in outer-doublet microtubule morphogenesis. J Cell Sci 118, 5421–5430.

Dymek EE, Smith EF (2007). A conserved CaM- and radial spoke–associated complex mediates regulation of flagellar dynein activity. J Cell Biol 179, 515–526.

Fu G, Wang Q, Phan N, Urbanska P, Joachimiak E, Lin J, Wloga D, Nicastro D (2018). The I1 dynein-associated tether and tether head complex is a conserved regulator of ciliary motility. Mol Biol Cell 29, 1048–1059.

Gorman DS, Levine RP (1965). Cytochrome f and plastocyanin: their sequence in the photosynthetic electron transport chain of *Chlamydomonas reinhardtii*. Proc Natl Acad Sci USA 54, 1665–1669.

Hagen WJH, Wan W, Briggs JAG (2017). Implementation of a cryo-electron tomography tilt-scheme optimized for high resolution subtomogram averaging. J Struct Biol 197, 191–198.

Harris E (1989). The Chlamydomonas Sourcebook, San Diego: Academic Press.
Heumann JM, Hoenger A, Mastronarde DN (2011). Clustering and variance maps for cryo-electron tomography using wedge-masked differences. J Struct Biol 175, 288–299.
Heuser T, Dymek EE, Lin J, Smith EF, Nicastro D (2012). The CSC connects three major axonemal complexes involved in dynein regulation. Mol Biol Cell 23, 3143–3155.
Heuser T, Raytchev M, Krell J, Porter ME, Nicastro D (2009). The dynein regulatory complex is the nexin link and a major regulatory node in cilia and flagella. J Cell Biol 187, 921–933.
Hoops HJ, Witman GB (1983). Outer doublet heterogeneity reveals structural polarity related to beat direction in *Chlamydomonas* flagella. J Cell Biol 97, 902–908.
Iancu CV, Tivol WF, Schooler JB, Dias DP, Henderson GP, Murphy GE, Wright ER, Li Z, Yu Z, Briegel A, *et al*. (2006). Electron cryotomography sample preparation using the Vitrobot. Nat Protoc 1, 2813–2819.
Ichikawa M, Liu D, Kastritis PL, Basu K, Hsu TC, Yang S, Bui KH (2017). Subnanometre-resolution structure of the doublet microtubule reveals new classes of microtubule-associated proteins. Nat Commun 8, 15035.
Ikeda K, Ikeda T, Morikawa K, Kamiya R (2007). Axonemal localization of *Chlamydomonas* PACRG, a homologue of the human *Parkin*-coregulated gene product. Cell Motil Cytoskeleton 64, 814–821.
Ikeda T (2008). *Parkin*-co-regulated gene (*PACRG*) product interacts with tubulin and microtubules. FEBS Lett 582, 1413–1418.
Kamiya R, Kurimoto E, Muto E (1991). Two types of *Chlamydomonas* flagellar mutants missing different components of inner-arm dynein. J Cell Biol 112, 441–447.
King SJ, Dutcher SK (1997). Phosphoregulation of an inner dynein arm complex in *Chlamydomonas reinhardtii* is altered in phototactic mutant strains. J Cell Biol 136, 177–191.
King SM (2016). Axonemal dynein arms. Cold Spring Harb Perspect Biol 8, a028100.
Kitada T, Asakawa S, Hattori N, Matsumine H, Yamamura Y, Minoshima S, Yokochi M, Mizuno Y, Shimizu N (1998). Mutations in the parkin gene cause autosomal recessive juvenile parkinsonism. Nature 392, 605–608.
Kremer JR, Mastronarde DN, McIntosh JR (1996). Computer visualization of three-dimensional image data using IMOD. J Struct Biol 116, 71–76.
Kubo T, Yanagisawa HA, Yagi T, Hirono M, Kamiya R (2010). Tubulin polyglutamylation regulates axonemal motility by modulating activities of inner-arm dyneins. Curr Biol 20, 441–445.
Lechtreck KF, Luro S, Awata J, Witman GB (2009). HA-tagging of putative flagellar proteins in *Chlamydomonas reinhardtii* identifies a novel protein of intraflagellar transport complex B. Cell Motil Cytoskeleton 66, 469–482.
Li X, Zhang R, Patena W, Gang SS, Blum SR, Ivanova N, Yue R, Robertson JM, Lefebvre PA, Fitz-Gibbon ST, *et al*. (2016). An indexed, mapped mutant library enables reverse genetics studies of biological processes in *Chlamydomonas reinhardtii*. Plant Cell 28, 367–387.
Lin J, Heuser T, Song K, Fu X, Nicastro D (2012). One of the nine doublet microtubules of eukaryotic flagella exhibits unique and partially conserved structures. PLoS One 7, e46494.
Lin J, Nicastro D (2018). Asymmetric distribution and spatial switching of dynein activity generates ciliary motility. Science 360, eaar1968.
Linck R, Fu X, Lin J, Ouch C, Schefter A, Steffen W, Warren P, Nicastro D (2014). Insights into the structure and function of ciliary and flagellar doublet microtubules: tektins, Ca^{2+}-binding proteins and stable protofilaments. J Biol Chem 289, 17427–17444.
Linck RW, Stephens RE (2007). Functional protofilament numbering of ciliary, flagellar, and centriolar microtubules. Cell Motil Cytoskeleton 64, 489–495.
Lorenzetti D, Bishop CE, Justice MJ (2004). Deletion of the Parkin coregulated gene causes male sterility in the *quaking*viable mouse mutant. Proc Natl Acad Sci USA 101, 8402–8407.
Maheshwari A, Obbineni JM, Bui KH, Shibata K, Toyoshima YY, Ishikawa T (2015). α- and β-Tubulin lattice of the axonemal microtubule doublet and binding proteins revealed by single particle cryo-electron microscopy and tomography. Structure 23, 1584–1595.
Mastronarde DN (2005). Automated electron microscope tomography using robust prediction of specimen movements. J Struct Biol 152, 36–51.
McVittie A (1972). Flagellum mutants of *Chlamydomonas reinhardtii*. J Gen Microbiol 71, 525–540.
Mendes Maia T, Gogendeau D, Pennetier C, Janke C, Basto R (2014). Bug22 influences cilium morphology and the post-translational modification of ciliary microtubules. Biol Open 3, 138–151.
Meng D, Cao M, Oda T, Pan J (2014). The conserved ciliary protein Bug22 controls planar beating of *Chlamydomonas* flagella. J Cell Sci 127, 281–287.
Mizuno K, Dymek EE, Smith EF (2016). Microtubule binding protein PACRG plays a role in regulating specific ciliary dyneins during microtubule sliding. Cytoskeleton 73, 703–711.
Nicastro D (2009). Cryo-electron microscope tomography to study axonemal organization. Methods Cell Biol 91, 1–39.
Nicastro D, Fu X, Heuser T, Tso A, Porter ME, Linck RW (2011). Cryo-electron tomography reveals conserved features of doublet microtubules in flagella. Proc Natl Acad Sci USA 108, E845–E853.
Nicastro D, Schwartz C, Pierson J, Gaudette R, Porter ME, McIntosh JR (2006). The molecular architecture of axonemes revealed by cryoelectron tomography. Science 313, 944–948.
Okagaki T, Kamiya R (1986). Microtubule sliding in mutant *Chlamydomonas* axonemes devoid of outer or inner dynein arms. J Cell Biol 103, 1895–1902.
Owa M, Uchihashi T, Yanagisawa HA, Yamano T, Iguchi H, Fukuzawa H, Wakabayashi KI, Ando T, Kikkawa M (2019). Inner lumen proteins stabilize doublet microtubules in cilia and flagella. Nat Commun 10, 1143.
Pettersen EF, Goddard TD, Huang CC, Couch GS, Greenblatt DM, Meng EC, Ferrin TE (2004). UCSF Chimera—a visualization system for exploratory research and analysis. J Comput Chem 25, 1605–1612.
Piperno G, Mead K, LeDizet M, Moscatelli A (1994). Mutations in the "dynein regulatory complex" alter the ATP-insensitive binding sites for inner arm dyneins in *Chlamydomonas* axonemes. J Cell Biol 125, 1109–1117.
Schneider CA, Rasband WS, Eliceiri KW (2012). NIH Image to ImageJ: 25 years of image analysis. Nat Methods 9, 671–675.
Segal RA, Huang B, Ramanis Z, Luck DJ (1984). Mutant strains of *Chlamydomonas reinhardtii* that move backwards only. J Cell Biol 98, 2026–2034.
Stoddard D, Zhao Y, Bayless BA, Gui L, Louka P, Dave D, Suryawanshi S, Tomasi RF, Dupuis-Williams P, Baroud CN, *et al*. (2018). *Tetrahymena* RIB72A and RIB72B are microtubule inner proteins in the ciliary doublet microtubules. Mol Biol Cell 29, 2566–2577.
Suryavanshi S, Edde B, Fox LA, Guerrero S, Hard R, Hennessey T, Kabi A, Malison D, Pennock D, Sale WS, *et al*. (2010). Tubulin glutamylation regulates ciliary motility by altering inner dynein arm activity. Curr Biol 20, 435–440.
Tam LW, Lefebvre PA (2002). The *Chlamydomonas* MBO2 locus encodes a conserved coiled-coil protein important for flagellar waveform conversion. Cell Motil Cytoskeleton 51, 197–212.
Thumberger T, Hagenlocher C, Tisler M, Beyer T, Tietze N, Schweickert A, Feistel K, Blum M (2012). Ciliary and non-ciliary expression and function of *PACRG* during vertebrate development. Cilia 1, 13.
West AB, Lockhart PJ, O'Farell C, Farrer MJ (2003). Identification of a novel gene linked to parkin via a bi-directional promoter. J Mol Biol 326, 11–19.
Wilson GR, Tan JT, Brody KM, Taylor JM, Delatycki MB, Lockhart PJ (2009). Expression and localization of the Parkin co-regulated gene in mouse CNS suggests a role in ependymal cilia function. Neurosci Lett 460, 97–101.
Wilson GR, Wang HX, Egan GF, Robinson PJ, Delatycki MB, O'Bryan MK, Lockhart PJ (2010). Deletion of the Parkin co-regulated gene causes defects in ependymal ciliary motility and hydrocephalus in the *quaking* viable mutant mouse. Hum Mol Genet 19, 1593–1602.
Wirschell M, Hendrickson T, Sale WS (2007). Keeping an eye on I1: I1 dynein as a model for flagellar dynein assembly and regulation. Cell Motil Cytoskeleton 64, 569–579.
Witman GB (1986). Isolation of *Chlamydomonas* flagella and flagellar axonemes. Methods Enzymol 134, 280–290.
Yanagisawa HA, Mathis G, Oda T, Hirono M, Richey EA, Ishikawa H, Marshall WF, Kikkawa M, Qin H (2014). FAP20 is an inner junction protein of doublet microtubules essential for both the planar asymmetrical waveform and stability of flagella in *Chlamydomonas*. Mol Biol Cell 25, 1472–1483.